Electrochimica Acta 362 (2020) 137111

Contents lists available at ScienceDirect

Electrochimica Acta

journal homepage: www.elsevier.com/locate/electacta

Uncovering the electrochemical interface of low-index copper surfaces in deep groundwater environments

Joakim Halldin Stenlid[a,1,*], Egon Campos dos Santos[a,b,1], Rosa M. Arán-Ais[c], Alexander Bagger[d], Adam Johannes Johansson[e], Beatriz Roldan Cuenya[c], Jan Rossmeisl[d], Lars Gunnar Moody Pettersson[a,*]

[a] Department of Physics, AlbaNova University Center, Stockholm University, SE-106 91 Stockholm, Sweden
[b] Departamento de Química, Universidade Federal de Minas Gerais, 31270-901 Belo Horizonte, MG, Brazil
[c] Department of Interface Science, Fritz Haber Institute of the Max Planck Society, 14195 Berlin, Germany
[d] Department of Chemistry, University of Copenhagen, Universitetsparken 5, 2100 Copenhagen, Denmark
[e] Swedish Nuclear Fuel and Waste Management Company (SKB), Evenemangsgatan 13, Box 3091, SE-169 03 Solna, Sweden

ARTICLE INFO

Article history:
Received 17 June 2020
Revised 12 August 2020
Accepted 11 September 2020
Available online 21 September 2020

Keywords:
Copper corrosion
DFT modeling
Cyclic voltammetry
Single-crystal surface
Ionic adsorption/desorption

ABSTRACT

Using a combination of a sophisticated modeling protocol and well-established electrochemical techniques, we unravel the chemical composition of the low-index surfaces of copper in groundwater environments at different ion concentrations, pHs, and redox potentials. By carefully linking density functional theory (DFT) and cyclic voltammetry (CV), we are able to extract fundamental information on interfaces of broad significance. Herein, we focus on the case of groundwater found in deep geological environments of importance to the planned constructions of disposal repositories for spent nuclear fuel around the world. Within the error margins of DFT, we can assign adsorption structures and compositions to the current peaks of the CVs. It is found that among the groundwater ions of main interest (i.e. sulfide, bisulfide, sulfate, chloride and bicarbonate), sulfides (HS^-, S^{2-}) bind strongest to the surface, and are likely to dominate at the interfaces under the deep geological conditions relevant for repositories of spent nuclear fuel.

1. Introduction

The electrified interface between the surface of an electrode and the liquid environment is central in many fields of science, including corrosion science, electrocatalysis, and nanochemistry [1–3]. The nanoscale structure and composition at the interface largely control the behavior of the material. Gaining access to atomically resolved information is thus often essential to properly understand and predict a material's properties. We have recently described a procedure built on joint experimental (cyclic voltammetry – CV) and theoretical (density functional theory – DFT) methods to provide detailed atomistic information on the electrochemical interface as a function of the local electrochemical environment [4–6]. The latter includes the effects of pH, redox potential (U), and the concentration of dissolved species. Here, we apply this procedure to obtain pH-, potential-, and concentration-resolved information on the atomic-scale nature of low-index copper surfaces in deep groundwater environments. By studying well-defined model surfaces experimentally and computationally, we are able to obtain a firm understanding of adsorbate interactions on copper that will serve as the basis for further studies of more complex and (arguably) more realistic systems. Our investigation is of relevance to numerous applications of copper, including plumbing, construction engineering, electronics, preservation of historical artifacts, and catalysis [7–9].

Of particular relevance is the application of copper as encapsulating material for disposal of spent nuclear fuel in deep geological repositories. This approach is considered by numerous waste management programs worldwide, including, e.g., the programs of Sweden, Canada, Taiwan and Finland [10–13]. A copper canister will act as one of several barriers to prevent the radioactive material from coming into contact with the biosphere. Historically, several materials have been considered for the encapsulation, e.g., carbon steel and stainless steel, titanium, Al_2O_3, and Cu–Ni alloys. Some of these materials are still under consideration in other repository programs. In general, the adequacy of an encapsulation material depends in a complicated way on several parameters, e.g.,

* Corresponding authors.
E-mail addresses: kjhstenlid@gmail.com, kjhs@kth.se (J. Halldin Stenlid), lgm@fysik.su.se (L.G.M. Pettersson).
[1] These authors have contributed equally.

https://doi.org/10.1016/j.electacta.2020.137111

the type of nuclear fuel, its degree of burnup, as well as the hydrogeology and geochemistry of the repository site. In the Swedish program, copper is chosen as canister material based on, among other properties, its corrosion behavior in comparison to other alternatives [14]. The other barriers, with assessed functionality of preventing and/or retarding the release of radionuclides, are the surrounding bedrock and a compacted bentonite clay buffer. Internal metallic structures of the copper canister, e.g., the zircalloy cladding of the fuel, and the load bearing cast iron insert, may also act as barriers to radionuclide release, as will the slow dissolution of the uranium oxide fuel itself, although the disposal systems are not designed to rely on the functionalities of these barriers. The radiation dose to humans and other organisms in the biosphere surface must remain below the level (or risk criterion) stipulated by national regulators (e.g., The Swedish Radiation Safety Authority, SSM), which are guided by international recommendations from institutions such as the International Atomic Energy Agency (IAEA). To fulfill such requirements, it is necessary that the outer canister material has sufficient resistance towards corrosive degradation by the local chemical environment that is in contact with the waste canister, which is essentially deep groundwater conditioned by bentonite clay. What is sufficient in terms of corrosion resistance depends on the performance of other barriers, as well as the geochemistry (e.g., concentration of sulfide) and hydraulic conductivity (groundwater flow) of the chosen site. The situation is complicated by the fact that the conditions vary over time (the typical assessment period for a repository is 10^5 years), but also between canister deposition positions within the repository [11]. In addition, the different repository sites around the world can have dissimilar preconditions. Altogether, this puts high demands on the flexibility of a model designed to predict the behavior and safety of the waste repositories.

For a comprehensive understanding of the behavior of copper in deep groundwater, copper as well as its corrosion products should be considered. In our previous work, we have addressed the aqueous interfaces of the Cu_2S corrosion product [6], whereas future studies should investigate the interfaces of Cu_2O. The present work focuses on metallic copper, with extrapolation into conditions where copper is known to oxidize but where metallic copper can be exposed in e.g. pore bottoms. The ambition of the present work is to investigate the atomic-scale response of the (100), (110), and (111) low-index surface facets of copper as the aqueous chemical environment is varied. This will be used as a basis to discuss the behavior of copper in groundwater environments. In particular, we here address, besides pH and potential effects, the effects of sulfide species (H_2S, HS^-, S^{2-}) and sulfate (SO_4^{2-}) anions. These are relevant species in numerous applications of copper. They are also present in the groundwater of Swedish, Finnish, and Canadian nuclear waste disposal sites, and are known to influence the corrosion behavior of copper. Other common groundwater species that are of interest in this respect are chloride (Cl^-) and bicarbonate (HCO_3^-). The latter two were included in our previous work [5], and we reanalyze the data to discuss the role of these anions in connection to the present work and the relation to deep geological groundwater environments. By building knowledge bottom up, and by ultimately including a large ensemble of surface facets, we can form the basis for a real, in-depth understanding of the copper material in aqueous environments.

2. Methods

2.1. Experimental

The electrochemical characterization of Cu single-crystal electrodes is described below. Cyclic voltammetries (CVs) of the Cu surfaces were performed at 50 mV/s in Ar-saturated (Air Liquide, N50) solutions containing 0.1 M NaOH (ACS. Reag., Merck), 0.1M NaOH + 10^{-5} M Na_2S ($Na_2S{\bullet}9H_2O$, 99.99 %, Sigma-Aldrich), 0.1M $HClO_4$ + 0.01M KCl (ACS. Reag. Merck) and 0.1M K_2SO_4 (ACS. Reag., Merck). Care was taken to keep the solutions oxygen-free by continuous bubbling with N_2. The electrode potential was controlled by a BioLogic 240 potentiostat in a three-electrode configuration, with a gold wire as a counter electrode and an Ag/AgCl reference electrode (CH Instruments, Inc.). Electrochemical measurements were carried out at room temperature in custom-made electrochemical cells. Before each measurement, the Cu single-crystal electrodes (MaTecK, 1 cm diameter, 99.999 %) with (100), (111) and (110) orientations were electropolished at 3 V vs. a Ti foil for 10 s in a solution consisting of 130 mL H_3PO_4 (VWR, 85 wt%), 20 mL H_2SO_4 (VWR, 95 wt%) and 60 mL ultrapure water (Elga, 18.2 MΩ cm). The electrodes were subsequently copiously rinsed with ultrapure water and rapidly transferred into the electrochemical cell, where CVs were recorded in a hanging meniscus configuration. This preparation protocol minimizes the amount of remaining surface oxides. However, although the Cu samples were always inserted into the solution at a controlled potential of −0.2 V_{RHE} at which Cu is expected to be reduced, trace amounts of oxide may still remain [15]. Previous investigations have shown that the voltammetric responses of single-crystal surfaces prepared by the herein employed electropolishing method closely match the responses of UHV-prepared samples [16], and our results fit well with previously published results [16–18]. Routine XRD and XPS of our samples further confirm the proper orientation and that the surfaces are free of contamination. Additional information about the experimental methods are given in the supporting information.

2.2. Computational

The computational details and theoretical framework are the same as described in our recent paper [6]. In brief, the procedure consists of computing the energies of a range of interface states consisting of different facets (100, 110, 111), and different adsorbates (H_2O, OH, O, H, H_2S, HS, S, SO_4, Cl) in aqueous environment with a varying degree of coverage and deprotonation. For this, we use DFT at the PBE+D3(BJ) level of theory [19–21] and the VASP program suit throughout [22]. For each state, the low-energy structure on a periodic six-layers-thick slab model with three additional layers of explicit water solvent molecules is first identified by starting from initial structures of varied orientation and adsorption positions. Thereafter, a range of different interface structures with varied water orientation is sampled dynamically with *ab initio* molecular dynamics (AIMD). Every structure gives rise to a different work function (W_F) and free energy (G=E_{DFT}+ZPE). Here G includes the DFT energy, E_{DFT}, and the zero-point energy (ZPE) obtained from vibrational analysis (as described in Ref. [23]) of the low-energy structures. The W_F is defined as

$$W_F = V_v - E_F/e \quad (1)$$

where V_V is the electrostatic potential in vacuum in close proximity to the surface (here taken as the potential of the vacuum space in between the periodic slabs using dipole corrections [24]) while E_F and e are the Fermi energy and elementary charge, respectively. The obtained W_F and G are related to the potential (U) and pH of the system by the use of two references: the computational hydrogen electrode [25] and the experimental value [26] of the work function of the standard hydrogen electrode ($W_{F,SHE}$ = 4.4 eV). Through the outlined procedure we can express the free energy for the interfacial system, G^{int}, via the so-called generalized computational hydrogen electrode (GCHE) [27] by

$$G^{int} = G(\Delta n) - G^{int}_{ref}(\Delta n = 0) - \Delta n \cdot \left(\frac{\mu^0_{H_2}}{2} - eU_{RHE} \right) \quad (2)$$

Here $\Delta n{=}n{-}n_0$, where n is the number of protons in the studied state and n_0 the number of protons in the pure water-copper reference state with energy G^{int}_{ref}. Hence Δn reflects the protonation/deprotonation of the system. In the reference state, n_0 is taken as the number of H in the water layer bonded to the surface, i.e. $2m$ with m being the number of surface adsorption sites, which is chosen as the number of available adsorption sites for water on each surfaces. For the slab models, a 2×3 surface supercell was used for the (100), (110), and (111) facets, leading to $m = 6$, 8, and 6, respectively. The standard chemical potential of H_2, $\mu^o_{H_2}$, is treated similarly as the other adsorbates (*vide infra*) with free-energy corrections taken from the NIST-JANAF tables [28]. The potential of the reversible hydrogen electrode (U_{RHE}), and standard hydrogen electrode (U_{SHE}), are related through

$$eU_{RHE} = eU_{SHE} + 2.3\,k_B T\,pH = W_F - W_{F,SHE} + 2.3\,k_B T\,pH \quad (3)$$

where T is the temperature (298.15 K) and k_B the Boltzmann constant. Adsorbates other than H_2O are included by relating the energies to the respective gas-phase molecules. For the sulfide species, H_2S(g) is used; for sulfate SO_3(g), and H_2O(g); and for HCl, HCl(g). The variations in H coverage are related to H_2(g). The total interface energy for the adsorbate system, G^{int}_{ads}, is evaluated by

$$G^{int}_{ads} = G^{\text{int}} - \overbrace{\Delta n_{H_2S}\,\mu_{H_2S} - \Delta n_{HS}\,\mu_{HS^-} - \Delta n_S\,\mu_{S^{2-}}}^{H_xS} - \overbrace{\Delta n_{Cl}\,\mu_{HCl}}^{Cl^-} - \overbrace{\Delta n_{SO_4}\cdot(\mu_{H_2O} + \mu_{SO_3})}^{SO_4^{2-}} \quad (4)$$

Where G^{int} is evaluated by Eq. (3). The chemical potential μ^o_i of the adsorbate reference molecules is composed of

$$\mu_i(T) = E_{DFT,i} + ZPE_i + \Delta\mu^0_i(T^0, p^0) + k_B T\,ln\left(\frac{K_{H,i}\,c}{p^0}\right) \quad (5)$$

for which all corrections to the standard state of 1 bar and 298.15 K are taken from the NIST-JANAF tables [28]. To correct to arbitrary concentrations, we use Henry's law to link the gas phase pressure to the given concentration using constants, $K_{H,i}$, obtained from the NIST-JANAF tables [28]. The standard vapor pressure of water at 298.15 K is used as partial pressure of H_2O. The final energies are normalized by the number of exposed copper atoms at the surfaces, i.e. 9, 8, and 12 for Cu(100), Cu(110), and Cu(111), respectively.

In all calculations the valence states were evaluated using a plane-wave basis set with a 400 eV cut-off, while the core states were represented by standard PAW [29,30] potentials. A Γ-centered $4 \times 4 \times 1$ **k**-point mesh was used and the energies and work-functions were evaluated using the Methfessel–Paxton [31] approach with a Gaussian width of 0.2 eV. The AIMD were run at the same level of theory for 1 ps with a time step of 1 fs, but using only the Γ-point and no dipole corrections. The aim of the AIMD is not necessarily to represent thermalized water, but rather to provide a range of structures representative of the interface with varying workfunction and corresponding energies that can be used to fit the linear GCHE equations. To be accurate, we have found the model system has to fulfill a few criteria: i) the start-structure must be well optimized (low-energy), and ii) the sampling has to be long enough and cannot drift. In this respect, we have previously found that 1 ps is sufficient for the sampling given well optimized low-energy interface start structures [6].

Simulated current densities, j, were obtained from the DFT-GCHE predicted surface charges $Q(V)$, which is a function of the potential-dependent coverage (Θ_i) of each state, i, as

$$j(V) = \frac{\partial Q(V)}{\partial t} = \frac{\partial Q(V)}{\partial V}\cdot\frac{\partial V}{\partial t} \quad (6)$$

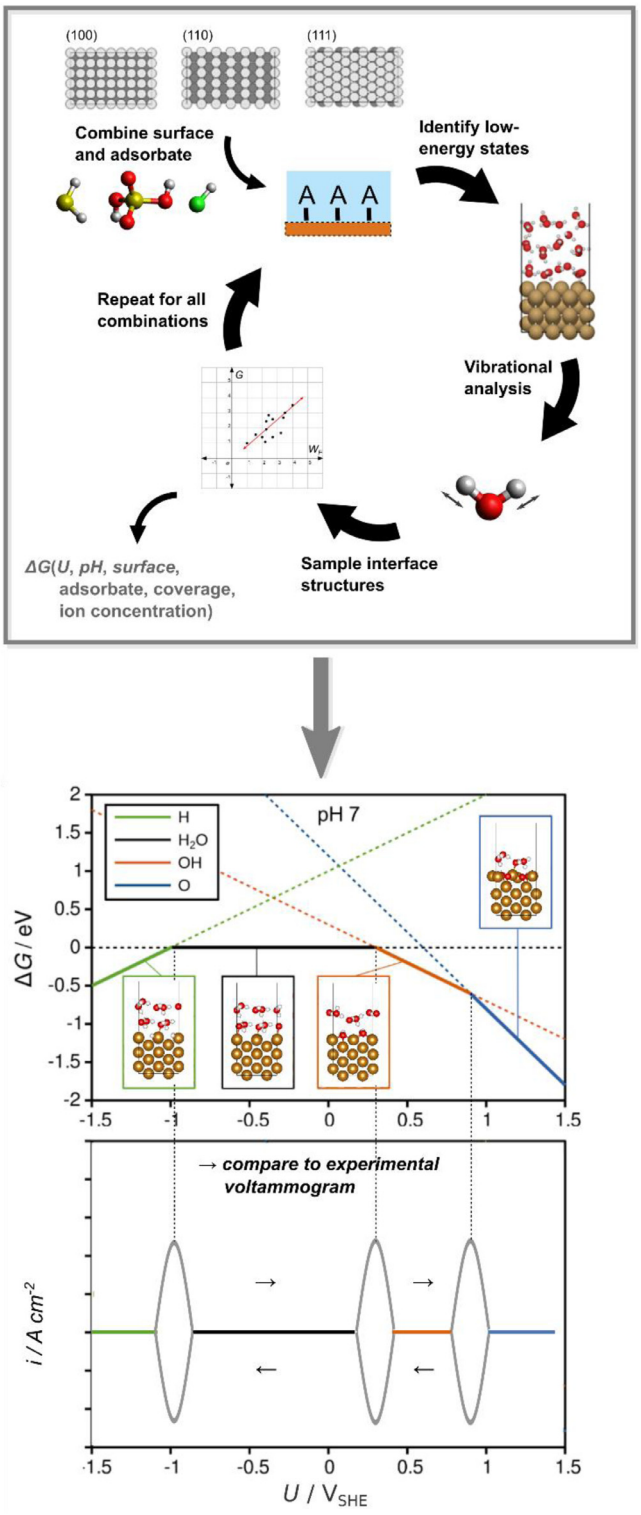

Fig. 1. Overview of the methods. The top figure illustrates the theoretical procedure to obtain pH-, *U*- and concentration-dependent free energies (ΔG) for the interface structures, further described in the methods section. Bottom figure, example of the resulting phase diagram in clean water at pH 7 showing free energy versus potential for the H, H_2O, OH, and O adsorbates. This can be translated to a simulated voltammogram [5], as a change in the surface charge (*cf.* coverage) leads to a current response. The simulated voltammogram can be directly compared to experiment.

$$Q(V) = \frac{1}{Z} \cdot \sum_i \theta_i \cdot Q_{ML} \cdot q_i \cdot e^{-\frac{E_i(V)}{k_B T}} \quad (7)$$

In the above, Z is the partition function, $\partial V/\partial t$ is the scan rate (50 mV/s in the current work), q_i the ionic charge of state i, k_B the Boltzmann constant, and T the temperature – assumed to be 298.15 K. Q_{ML} is the charge density of the Cu-facets with a monovalent ion adsorbed on all exposed Cu atoms. For fcc Cu, with a lattice constant of 3.615 Å, Q_{ML} is 245, 347, and 283 μC cm^{-2} for Cu(100), Cu(110), and Cu(111), respectively (i.e., elementary charge × surface Cu density).

3. Results and discussion

Our approach is based on a combination of experimental cyclic voltammetry (CV) and periodic DFT calculations employed within the framework of the generalized computational hydrogen electrode (GCHE) [27]. Details are given in the methods section, and illustrated in Fig. 1. The experimental CVs are first recorded in 0.1M NaOH solution in order to confirm the surface characteristics of the copper (100), (110), and (111) electrodes after the electropolishing treatment, and then conducted at low concentrations of sulfur to pin-point the adsorption/desorption events of ionic species at these surfaces as the surface potential (voltage) is varied. Cyclic voltammetry in alkaline electrolyte can be used as a reliable technique to check the preferential surface orientation of Cu single-crystal electrodes, as well as for the identification of surface defects [32]. Any adsorption/desorption process giving rise to charging/discharging of the interface is tracked by a corresponding current density response – a peak – in the voltammograms. From the DFT-GCHE simulations, we obtain information on the coverage of adsorbed (charged) species at any given potential. Through this approach, we can thus link changes in the preferred surface coverage identified by DFT-GCHE with the responses in the experimental voltammograms.

3.1. Sulfide and sulfate electrolytes

In our previous studies, we have demonstrated that for the entire pH spectrum – going from acidic, to neutral, and alkaline electrolytes, including chloride, carbonate, and sodium hydroxide – we are able to link the measured CV features to changes in the modeled interfacial composition as a function of the potential [5]. Herein we present extended results for new adsorbates of similar accuracy as in our previous work. Our investigation leads to good agreement between theory and experiment in almost all studied cases, with an estimated error margin of approximately ±0.2 V when comparing measured CV peak positions with predicted positions from the DFT-GCHE simulations. This resolution is in the current application good enough to assign most of the CV peaks based on the DFT structures.

Fig. 2 and Fig. 3 contain measured voltammograms (bottom row) for 50 μM Na_2S +0.1 M NaOH (pH 13) and 0.1 M K_2SO_4 (pH 8.7) electrolytes, respectively, on the low-index copper surfaces. Included are also simulated CVs (middle row), and the corresponding DFT-GCHE prevalence diagrams (top row). In these diagrams, the most favorable state – and hence the prevailing state – at a given potential (U) is the state of lowest Gibbs free energy. We focus on a potential interval ranging from −0.25 to 0.4 V_{RHE}. This roughly corresponds to the stability region (including kinetic effects and overpotential) between H_2 evolution resulting from water splitting at the lower end, and copper oxidation at the higher end. In the current work, we have only considered pure adsorption states explicitly, i.e. mixed adsorption of, e.g., S* and Cl* or S* and OH* are not included.

As seen in Figs. 2 and 3 (top rows), the Cu surfaces are covered by adsorbed water (H_2O^*) mixed with sulfate (SO_4^*) or sulfide (S*), depending on the applied electrolyte, over most of the considered potential range. The clear exception is Cu(110) for which SO_4^* is not adsorbed (Fig. 3, middle panel) at intermediate potentials due to a favored dissociated water phase (0.25ML OH*/H*) on the corrugated Cu(110) surface [33,34]. This is not the case on the (100) and (111) facets where the adsorption of dissociated water is much weaker (Fig. 3, left and right panel).

We perform a more detailed analysis below. Our analysis goes from low to high potentials as the simulated CVs correspond better to the anodic trace (negative to positive potential) of the experimental CVs. This is due to asymmetries in the experimental CV peaks caused by mass transportation/kinetic effects [35], in combination with film growth at higher potentials. In the anodic direction adsorption/desorption occurs from an (approximately) clean surface, whereas this is not necessarily true in the cathodic direction. At the lowest considered potentials (below −0.25 V_{RHE}), DFT-GCHE suggest that H* is the thermodynamically favored adsorbate in all the studied cases (Fig. 2, top row). However, H_2(g) is more stable (at pressures below and around 1 bar) and H_2 generation will occur at potentials below 0.0 V_{RHE}. In line with this, a recent study on purely water-covered surfaces suggests that if kinetic effects are included in the analysis, the H-coverage will tend towards zero [16]. Therefore, the DFT-predicted transition from H* to H_2O^* or to mixed OH*/H* phases will not be detectable in the experimental CVs. Thus, we omit H* from the analysis (expet for OH*/H* states) and interpret all low-potential peaks that arises with increased potential as being the transition from H_2O^* going to an anion-covered surface.

As the potential is increased from −0.25 V_{RHE} in the sulfate or sulfide electrolytes, any species (H*, OH*, and/or H_2O^*) persisting on the surface will eventually be replaced by SO_4^* or S*.[1] For Cu(110), this transition first passes through a mixed H* and OH* phase (Figs. 2 and 3, middle panel). The adsorption of SO_4^* or S* leads to a build-up of negative charge (or reduction of positive charge) at the interface. The CV peak corresponding to this transition is seen in the experiment for some cases, i.e. for S* on Cu(100) as well as for SO_4^* on Cu(111), see Fig. 2 (left panel, bottom row) and Fig. 3 (right panel, bottom row). For the other cases, the transition appears to be masked in the experimental CVs by the H_2-evolution region and/or occur at potentials lower than those recorded in the CVs.

For the low-potential region, we draw the following conclusions: in sulfide solutions, the peak at −0.12 V_{RHE} in the experimental CV for Cu(100) is attributed to the transition H_2O^* to ½ ML S* (Fig. 2, left panel, bottom row). Based on the DFT-GCHE results, we believe that the ambiguous small peaks around −0.1 V_{RHE} in the experimental CVs for Cu(110) and Cu(111) (Fig. 2, middle/right panels, bottom row) also correspond to a H_2O^* to ½ ML S* transition, although these peaks are largely masked by the H_2 evolution in the experiment. In the case of sulfate, the lack of a low-potential peak on Cu(100) in the experiment (Fig. 3, left panel, bottom row), and the relatively favored interaction predicted by DFT-GCHE, suggest that the surface is covered by a 1/3 ML of SO_4^* already at potentials lower than −0.25 V_{RHE}. On Cu(111) (Fig. 3, right panel, bottom row) the transition from H_2O^* to 1/3 ML SO_4^* occurs at −0.20 V_{RHE} in the experiments (−0.1 V_{RHE} in DFT-GCHE), whereas on Cu(110) (Fig. 3, middle panel, bottom row) a favorable mixed OH*/H* phase delays the adsorption of SO_4^* to higher potentials (*vide infra*).

For higher potentials, large differences in the influence of sulfate and sulfide on the voltammograms (and interface charac-

[1] We find that HS* will not be favored on the surfaces.

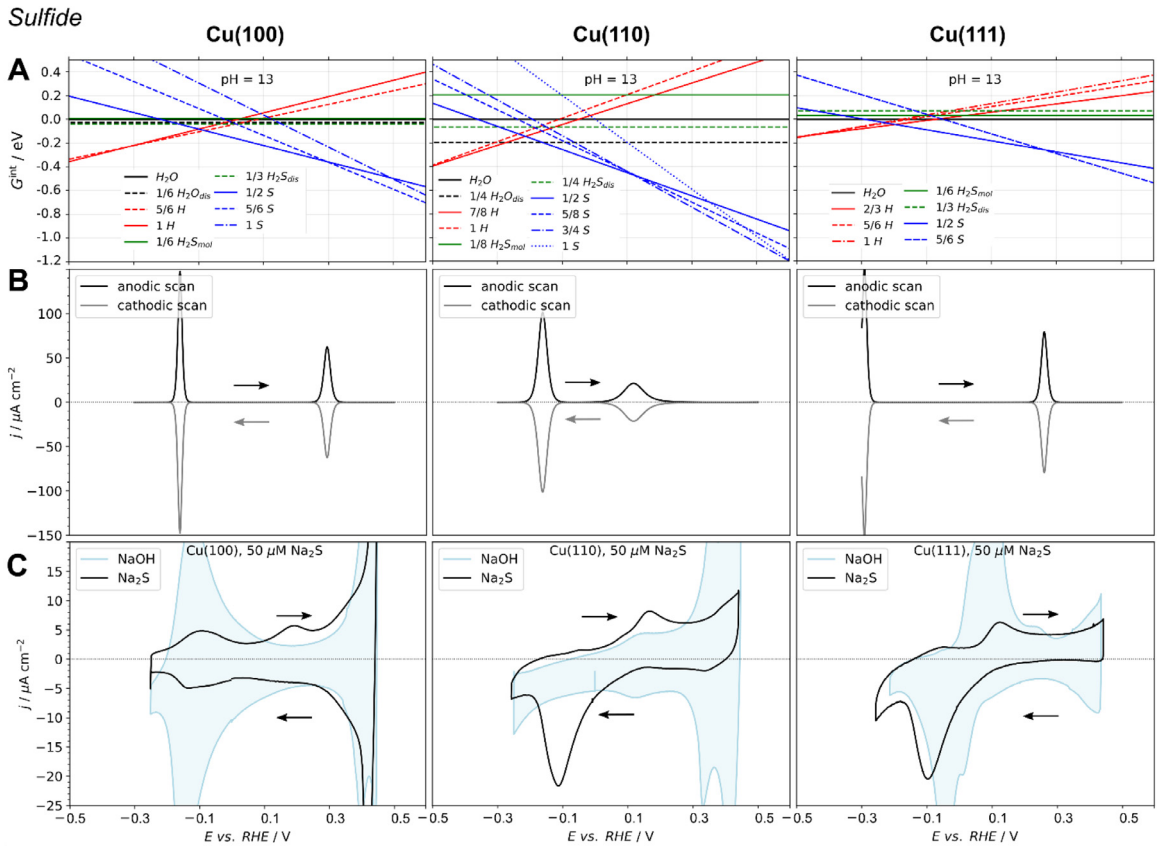

Fig. 2. A) Computed (DFT-GCHE) prevalence diagrams for sulfide electrolytes as a function of the potential. B) The corresponding simulated CV omitting contributions from H*. C) Experimentally recorded CVs in a 50 μM Na_2S + 0.1 M NaOH electrolyte compared to CVs in a NaOH electrolyte. Note that the comparison between experimental and simulated CVs is most accurate in the positive sweep direction due to the asymmetric redox peaks. CVs for polycrystalline copper and for extended anodic potentials ranges are included in Figs. S1 and S2. All data obtained at pH 13.

teristics) are seen. For SO_4*, the main part of the experimental voltammograms from approximately −0.2 V_{RHE} is flat (i.e. no current and no charging/discharging), see Fig. 3, bottom rows. This is typically the case up until the onset of copper oxide formation, which occurs at around 0.3–0.4 V_{RHE}. In contrast, there are a number of broad peaks appearing in the sulfide solutions (Fig. 2, bottom rows), as will be discussed below. However, before this we note a few points of interest for SO_4*. Firstly, the adsorption of SO_4^{2-} obviously suppresses the experimental CV responses in the low to intermediate potential range (up to 0.2 V_{RHE}) seen in pure NaOH electrolytes: e.g., the typical OH adsorption peak on Cu(100) and at around -0.15 V_{RHE}, what is often inferred as surface (hydr)oxidation-induced reconstruction of Cu(111) at around 0.05 V_{RHE}, see Fig. 3 (bottom row). On the other hand, new distinct features not seen in the NaOH electrolytes appears in the K_2SO_4 electrolytes just before the oxidation leading to copper oxide on all the surfaces at potentials around 0.2–0.4 V_{RHE}. We note, also, that the effect of the cation, K^+ or Na^+, on the CV features is negligible as judged by comparison to previously recorded CVs [5,16,18]. The new peaks fit well with the increase in SO_4* coverage predicted by DFT-GCHE at these potentials in the case of Cu(100) and Cu(111), see Fig. 3, left/right panels, top row. For Cu(110), DFT-GCHE suggests that the new features correspond to the replacement of the mixed H*+OH* surface phase by SO_4* (Fig. 3, middle panel, top row). It is also possible that SO_4*, to a certain degree, promotes oxide formation, and that the new features in part reflect an earlier onset of the oxidation process.

As mentioned above, the sulfides influences the voltammograms significantly (Fig. 2, bottom row), and causes broad oxidation peaks starting already at low potentials. This is in line with the fact that sulfide is known to corrode copper via

$$2Cu + HS^- + H_2O \rightarrow Cu_2S + OH^- + H_2(g). \quad (8)$$

with a standard equilibrium potential of −0.89 V_{SHE} for the Cu/Cu_2S couple [36], and typical corrosion potentials of −0.7 to −0.4 V_{SHE} (i.e. 0.07 to 0.37 V_{RHE} at pH 13) for μM solutions.[36–39] Our results suggest that sulfide-species cover the surface well below the standard redox and corrosion potentials: already at −0.3 to −0.2 V_{RHE}, a sub-monolayer (≤ ML) of S* replaces H_2O* or H*+OH* (alternatively H*) on all the surfaces according to the DFT-GCHE data (Fig. 2, top row). The broad peaks seen in the experimental CVs starting in this potential range can thus be interpreted as a slow sequential growth of a sub-monolayer sulfide film, or alternatively due to the slow kinetics for reorganizing the surfaces to best accommodate S*. On all surfaces, a sharper peak arises around 0.1 to 0.2 V_{RHE} in the experimental CVs (Fig. 2, bottom row). The peak appears earliest for Cu(111), and latest for Cu(100). The rise of the peak fits well with the DFT-GCHE picture that indicates the formation of a ML of S* (Fig. 2, left/right panels, top row). The position of this peak coincides with the corrosion potential of copper in sulfide solutions, and with the region of Cu_2S formation found in other studies [40–42]. Beyond this peak, the experimentally observed increased current density (Fig. 2, bottom row), starting at around 0.3–0.4 V_{RHE}, likely corresponds to continued copper sulfide (Cu_2S and CuS) growth, followed by (hydr)oxide film growth at somewhat higher potentials [40–42]. See also Fig. S1 showing CVs recoded for an extended potential range.

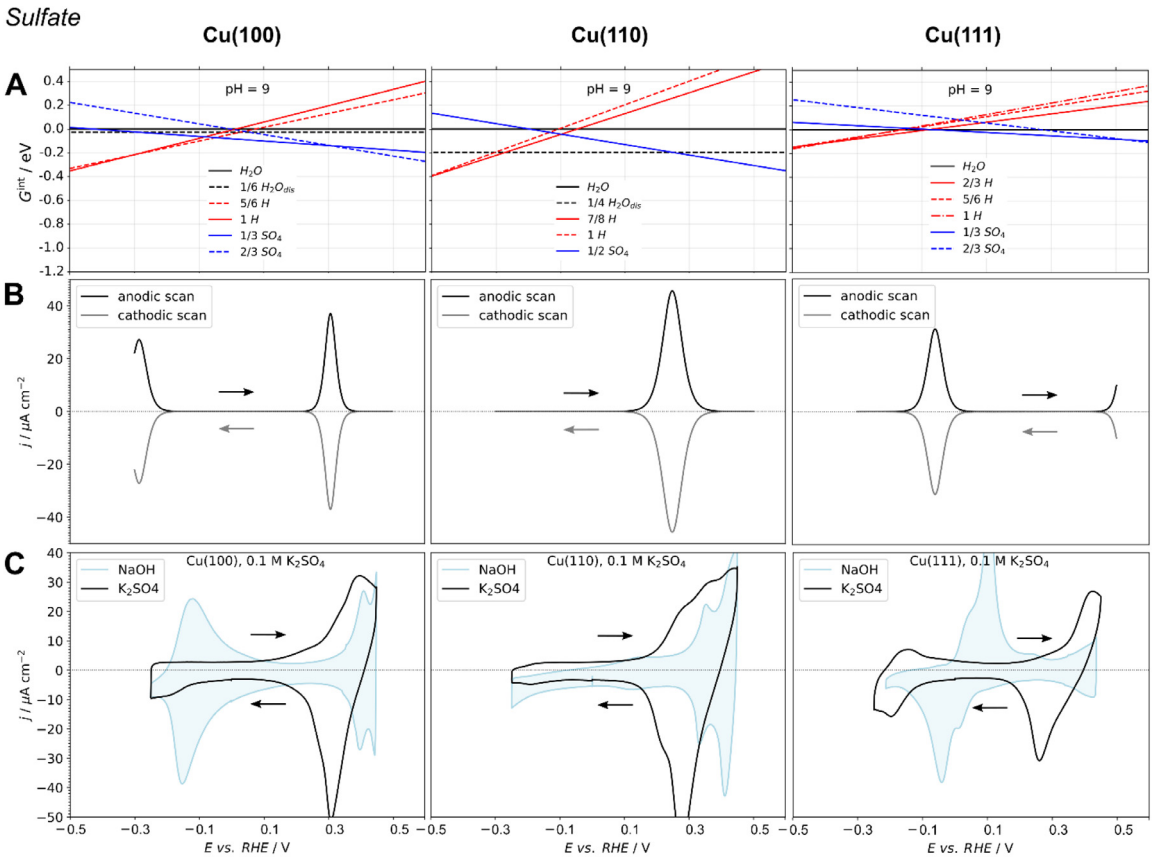

Fig. 3. A) Computed (DFT-GCHE) prevalence diagrams for sulfate electrolytes as a function of the potential. B) The corresponding simulated CV omitting contributions from H*. C) Experimentally recorded CVs in a 0.1 M K_2SO_4 electrolyte compared to CVs in a NaOH electrolyte. Note that the comparison between experimental and simulated CVs is most accurate in the positive sweep direction due to the asymmetric redox peaks. All data obtained at pH 9.

3.2. Comparison to chloride and carbonate electrolytes

We have previously studied the interactions of chloride and carbonate on surfaces of copper [5,6]. These ions are both present in typical groundwater environments and are known to affect the corrosion behavior (e.g., corrosion morphology) of metals in general, also including copper [43–46]. Our analysis has shown that chloride binds strongly to copper surfaces and largely affects the experimental CVs. In contrast, carbonate (and bicarbonate) interacts rather weakly with the surface. For this reason, carbonate will most likely be suppressed at the interface by the other ions present in the groundwater environments (in particular bisulfide, sulfate, and chloride), as indicated by our previous investigations [6]. Therefore, carbonate will not be considered further in the present work. In contrast, and for completeness, we revisit chloride computationally using the same level of theory as for sulfate and sulfide. Thereby, we can thus compare these ions on an equal footing. Fig. 4 shows the surface prevalence diagrams (top row) and simulated CVs (middle row) for Cl^- solutions compared to the experimental voltammograms in 0.01 M KCl (and 0.1 M $HClO_4$) from Ref. [5] (bottom row).

Our data suggest that Cl^- and SO_4^{2-} have very similar adsorption behavior. The difference is that Cl forms one ML whereas SO_4 forms a ⅓ML, leading to a higher net charge of the Cl interfaces. Thus, the stability of Cl will increase more steeply with higher potentials. As for SO_4, the combined information from the experimental CVs and the DFT-GCHE results indicates that Cl will cover the surfaces already at potentials below −0.25 V_{RHE} on Cu(100) and Cu(111) (Fig. 4, left/right panels, top row). Thus, no peaks are seen in the voltammograms corresponding to $H_2O^* \rightarrow Cl^*$ (Fig. 4, left/right panels, bottom row). On Cu(110), Cl^* adsorption is outcompeted at intermediate potentials due to the favorable mixed OH^*/H^* phase (Fig. 4, middle panel, top row) – similar to what was found for sulfate on Cu(110). The OH^*/H^* phase is replaced by Cl^* at around 0.13 V_{RHE}, which is seen clearly in the voltammogram (Fig. 4, middle panel, bottom row). This interpretation differs from our recent work [5], in which we did not account for the possibility of forming a mixed OH^*+H^* layer. We can also note that the main copper oxidation peak occurs earlier (at *ca.* 0.2 V_{RHE}) for the chloride solutions than for the other studied solutions. This is indicative of the potency of Cl^- as corrosion promotor and the thermodynamic fact that Cu bulk corrosion occurs at a lower V_{RHE} at acidic pH as compared to neutral and alkaline. Copper corrosion at low pH leading to dissolved Cu^{2+}(aq) complexes is a pH-independent process, whereas corrosion at neutral and alkaline conditions leading to the formation of Cu_2O(s) is pH-dependent [47]. Therefore, on the pH-dependent V_{RHE} scale, the oxidation peak will (theoretically) occur at constant potential in alkaline pH conditions. From pH 6–7, and below, the oxidation peak still occurs, but at decreasingly lower potentials.

3.3. Relation to groundwater environments in deep geological repositories

The above results can be related to the groundwater environments of the planned spent nuclear fuel sites around the world. Table 1 summarizes representative concentrations for the sulfide, sulfate, chloride, and carbonate groundwater ions in Sweden/Finland and Canada [11,38,48]. Whereas Sweden and Finland have decided on the specific site, the Canadian program is in the

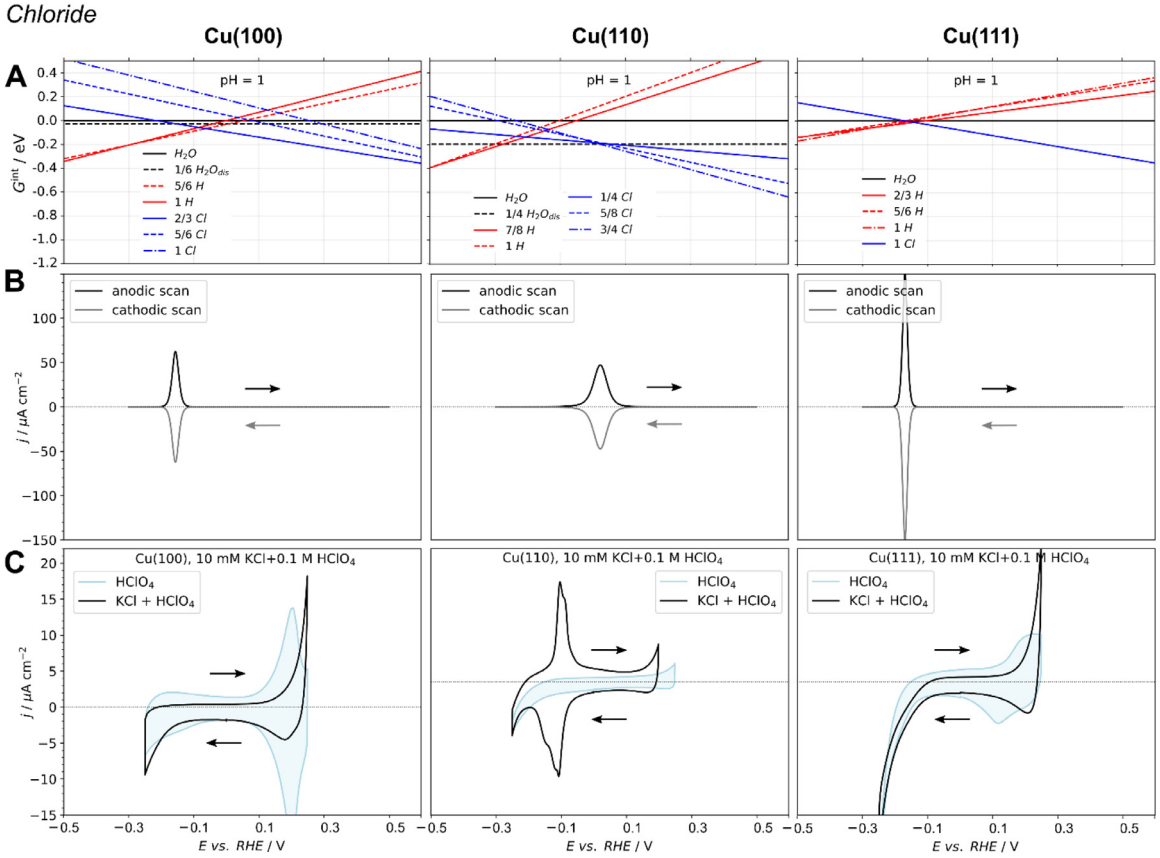

Fig. 4. A) Computed (DFT-GCHE) prevalence diagrams for chloride-containing electrolytes as a function of the potential. B) The corresponding simulated CV omitting contributions from H*. C) Experimentally recorded CVs in a 10 mM KCl + 0.1 M $HClO_4$ electrolyte compared to CVs in a $HClO_4$ electrolyte. All data obtained at pH 1.

Table 1
Representative anion groundwater concentrations in planned Swedish [11,38] and Canadian [48] spent nuclear fuel (SNF) repositories.

Species	Concentration	
	Sweden/Finland (granite)	Canada (sedimentary rock)
$[H_2S]+[HS^-]$	10 μM	10 nM
$[Cl^-]$	0.1 M	5 M
$[SO_4^{2-}]$	5 mM	5 mM
$[HCO_3^-]+[CO_3^{2-}]$	2 mM	0.1 mM

process of choosing between different sites. For Canada, we have included the case of a sedimentary rock site that has a notably lower sulfide concentration (around 1000 times lower), but higher chloride concentration (ca. 50 times higher) than the Swedish and Finnish sites. While the chosen sulfide concentration of 10 μM is representative for the Olkiluoto site in Finland, this value is at the high end of the distribution of sulfide concentrations measured at the Forsmark site in Sweden [49]. Based on these concentrations and the DFT-GCHE data, we can construct interface prevalence diagrams over a range of pHs and potentials – i.e. Pourbaix diagrams. These are shown in Fig. 5. H* is included in these diagrams because the cathodic H_2 evolution is expected to be relatively slow under the repository conditions, as is the entire copper corrosion process [50] – thus allowing for the build-up of H* at the interfaces. The reader should note that the diagram extrapolates into condition regimes where metallic copper is expected to be oxidized to copper (hydr)oxides or sulfides. However, these surface phases are not accounted for in Fig. 5, in order to highlight the interfacial composition for metallic copper (momentarily) exposed in, e.g., pore bottoms or cracks.

To use the Pourbaix diagrams of Fig. 5, we need to know the relevant pH and potential ranges. When initially entrapped O_2 in the bentonite clay has been depleted by copper corrosion and other processes, and the sulfidic groundwater has had time to diffuse through the clay barrier, the potential at the copper surface in the groundwater is expected to be dictated by sulfide-induced corrosion of Eq. (8) that can be divided into its half-cell reactions: [50]

$$\text{Anode}: 2Cu(s) + OH^- + HS^- \rightarrow Cu_2S(s) + H_2O + 2e^- \quad (9)$$

$$\text{Cathode}: 2H_2O + 2e^- \rightarrow H_2 + 2OH^- \quad (10)$$

$$\text{Total}: 2Cu(s) + HS^- + H_2O \rightarrow Cu_2S(s) + H_2(g) + OH^-$$

The corrosion potential (E_{corr}) for this process lies between −0.7 V_{SHE} and −0.4 V_{SHE} for Swedish/Finnish and Canadian conditions, with lower sulfide concentration leading to a higher expected E_{corr} [36–39]. The pH will likely be in the range 7–9 [51,52].

Given the expected conditions, the Pourbaix diagrams predict that mainly S* covers the surfaces. However, for both the Swedish/Finnish and the Canadian cases, the region with dominating H* also lies within the expected pH and potential ranges. Hence, it is possible that the surface has a mixed S* and H* coverage. This is of course perfectly in line with the fact that the corrosion potential balances between the cathodic H_2-evolution, that passes through an H* intermediate, and the anodic copper sulfide production that includes S* as transient species [50]. In addition, there are some small differences between the different copper facets, where, e.g., H* has a larger stability relative to S* on the Cu(100) facet compared to on Cu(110) and Cu(111). We note,

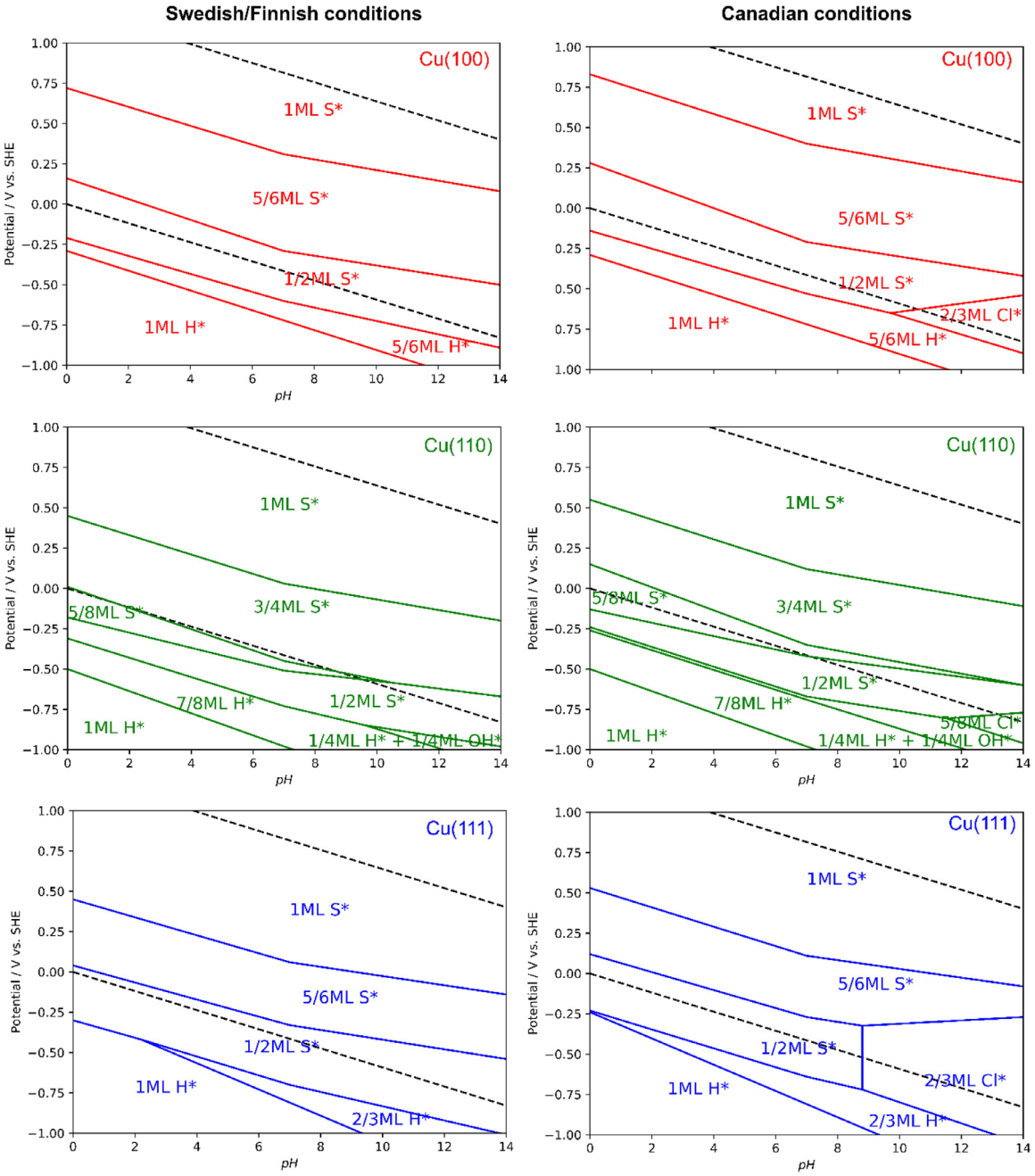

Fig. 5. Computed surface Pourbaix diagrams for metallic copper showing the prevalent interface phase as a function of the pH and redox potential under Swedish/Finnish and Canadian spent nuclear fuel repository conditions. Note that while we estimate a (conservative) error margin of 0.2 eV for our methods, the correspondence between simulated and experimental CVs in, e.g., Fig. 2 indicate a smaller discrepancy. Note, also, that the diagrams do not take into account bulk oxidation of copper.

in passing, that this might suggest that Cu(100) has a larger tendency to be cathode, while Cu(110) and Cu(111) are instead anodes, during corrosion. Overall, our data is in close agreement with the Pourbaix diagrams reported by Protopopoff and Marcus for polycrystalline Cu in sulfidic media [53].

There are also minor differences between the Canadian and the Swedish/Finnish environments. The H*/S* preference will not be altered significantly as the stability of both H* and S* is expected to directly follow the change in E_{corr} since the charging at the interface is approximately the same (1/2 ML S* versus ~1 ML H*). However, the enhanced Cl* prevalence for Canadian conditions compared to Swedish/Finnish is noteworthy. In the former case, Cl* is not expected to outcompete S* at the most likely pH of 7–9, but, in particular on the Cu(111) surface, Cl* is predicted to cover the surface at pH $\geq$ 9. From this one could thus speculate that it is possible that a mixed S* and Cl* phase is preferred also at lower pH, however, this analysis is beyond the scope of the present paper. Based on the above, it is likely that Cl* to some degree will influence the corrosion behavior of copper in the spent nuclear fuel repository environment. The more alkaline conditions, the more pronounced will this effect be.

Finally, the differences between adsorption behavior of the studied anions on the different facets of Cu provide a possible explanation to the observed differences between the corrosion behavior of copper when exposed to different ionic solutions. In particular, it has been found that the corrosion rate and the morphology of the formed Cu_2S corrosion film vary largely with the dissolved ions and their concentrations [6,44,45,54]. Species ad-

sorbed on the Cu surface can promote or inhibit corrosion and film growth. The facet-dependent adsorption information provided by the present study may serve as a basis for explaining local effects on the observed corrosion behavior.

4. Conclusion

In summary, ionic adsorption/desorption interactions on low-index interfaces of copper for application in deep groundwater environments have been studied using a combination of cyclic voltammetry and electrochemical DFT. It is demonstrated that the combined experimental and computational approach gives an enhanced understanding of the atomic-level details at the electrified interface between copper and aqueous solutions containing sulfide, sulfate and chloride anions. We conclude, in general, that all the studied anions replace water/protons at the interface at potentials around and above the reversible hydrogen-electrode reference potential with slight facet-dependent differences. We can also conclude that sulfide is the dominating adsorbed species at conditions expected in deep geological environments, with possible competition of adsorbed chloride and/or hydrogen. The present study provides basic insight into the behavior of well-defined copper surfaces of general interest for applications in aqueous surroundings.

Credit author statement

Joakim Halldin Stenlid: Writing - Original draft, Investigation, Formal analysis, Methodology, Visualization, Funding acquisition, Project administration; **Egon Campos dos Santos**: Writing - Review & Editing, Investigation, Formal analysis, Methodology, Software, Funding acquisition; **Rosa M. Arán Ais**: Writing - Original Draft, Investigation, Formal analysis; **Alexander Bagger**: Conceptualization, Software, Methodology, Validation, Writing - Review & Editing; **Adam Johannes Johansson**: Funding acquisition, Writing - Review & Editing, Validation, Conceptualization; **Beatriz Roldan Cuenya**: Writing - Review & Editing, Resources, Supervision; **Jan Rossmeisl**: Conceptualization, Methodology, Supervision, Funding acquisition; **Lars Gunnar Moody Pettersson**: Writing - Review & Editing, Resources, Funding acquisition, Supervision.

Declaration of Competing Interest

The authors declare that they have no known competing financial interests or personal relationships that could have appeared to influence the work reported in this paper.

Acknowledgments

This research was funded by the Swedish Nuclear Fuel and Waste Management company (SKB). RAA and BRC thank the financial support of the European Research Council (ERC-725915, OPERANDOCAT). LGM and ECS gratefully acknowledge support from the Swedish Energy Agency (Project 42024-1) as well as financial support provided by the Brazilian agencies: Fundação de Amparo à Pesquisa do Estado de Minas Gerais (FAPEMIG), Conselho Nacional para o Desenvolvimento Científico e Tecnológico (CNPq) and Coordenação de Aperfeiçoamento de Pessoal de Ensino Superior (CAPES). AB and JR acknowledge the Center for High Entropy Alloy Catalysis funded by the Danish National Research Foundation (DNRF 149). The calculations were performed using resources provided by the Swedish National Infrastructure for Computing (SNIC) at the PDC center. Computational resources provided through the Dellingr project of the Nordic e-Infrastructure Collaboration (NeIC) and CSC –IT Center for Science, Finland – are also gratefully acknowledged. We thank Christina Lilja and professor David Shoesmith for fruitful discussions.

Supplementary materials

Supplementary material associated with this article can be found, in the online version, at doi:10.1016/j.electacta.2020.137111.

References

[1] F.J. Vidal-Iglesias, R.M. Arán-Ais, J. Solla-Gullón, E. Herrero, J.M. Feliu, Electrochemical characterization of shape-controlled Pt nanoparticles in different supporting electrolytes, ACS Catal. 2 (2012) 901–910, doi:10.1021/cs200681x.
[2] V. Climent, J.M. Feliu, Thirty years of platinum single crystal electrochemistry, J. Solid State Electrochem. 15 (2011) 1297, doi:10.1007/s10008-011-1372-1.
[3] J.K. Nørskov, F. Studt, F. Abild-Pedersen, T. Bligaard, Energy trends in catalysis, in: Fundamental Concepts in Heterogeneous Catalysis, John Wiley & Sons, Inc, Hoboken, 2014, pp. 85–96, doi:10.1002/9781118892114.ch6.
[4] A. Bagger, I.E. Castelli, M.H. Hansen, J. Rossmeisl, Fundamental atomic insight in electrocatalysis, in: Handbook of Materials Modeling, Springer, Cham, 2018, pp. 1–31, doi:10.1007/978-3-319-50257-1_8-1.
[5] A. Bagger, R.M. Arán-Ais, J. Halldin Stenlid, E. Campos dos Santos, L. Arnarson, K.D. Jensen, M. Escudero-Escribano, B. Roldan Cuenya, J. Rossmeisl, Ab initio cyclic voltammetry on Cu(111), Cu(100) and Cu(110) in acidic, neutral and alkaline solutions, ChemPhysChem 20 (2019) 1–11, doi:10.1002/cphc.201900509.
[6] J.H. Stenlid, E.C. Dos Santos, A. Bagger, A.J. Johansson, J. Rossmeisl, L.G.M. Pettersson, Electrochemical Interface during corrosion of copper in anoxic sulfide-containing groundwater—a computational study, J. Phys. Chem. C 124 (2020) 469–481, doi:10.1021/acs.jpcc.9b08657.
[7] C. Leygraf, I. Odnevall Wallinder, J. Tidblad, T.E. Graedel, Atmospheric Corrosion, 2nd ed., John Wiley & Sons, Hoboken, NJ, 2016.
[8] K.P. Kuhl, E.R. Cave, D.N. Abram, T.F. Jaramillo, New insights into the electrochemical reduction of carbon dioxide on metallic copper surfaces, Energy Environ. Sci. 5 (2012) 7050–7059, doi:10.1039/C2EE21234J.
[9] Y. Hori, A. Murata, R. Takahashi, Formation of hydrocarbons in the electrochemical reduction of carbon dioxide at a copper electrode in aqueous solution, J. Chem. Soc., Faraday Trans. 85 (1989) 2309–2326 1, doi:10.1039/F19898502309.
[10] D.S. Hall, P.G. Keech, An overview of the Canadian corrosion program for the long-term management of nuclear waste, Corros. Eng. Sci. Technol. 52 (2017) 2–5, doi:10.1080/1478422X.2016.1275419.
[11] SKBLong-Term Safety for the Final Repository for Spent Nuclear Fuel at Forsmark: Main Report of the SR-Site Project, Swedish Nuclear Fuel and Waste Management Co, 2011 TR-11-01.
[12] POSIVA, SKBSafety Functions, Performance Targets and Technical Design Requirements for a KBS-3V Repository: Conclusions and Recommendations From a Joint SKB and Posiva Working Group, Posiva Oy and Swedish Nuclear Fuel and Waste Management Co, 2017 Posiva SKB Report 01.
[13] Oy Posiva, Safety Case for the Disposal of Spent Nuclear Fuel at Olkiluoto – Synthesis, Posiva Oy, Olkiluoto, Finland, 2012 POSIVA 2012-12.
[14] F. King, C. Padovani, Review of the corrosion performance of selected canister materials for disposal of UK HLW and/or spent fuel, Corros. Eng. Sci. Technol. 42 (2011) 82–90, doi:10.1179/174327821 1Y.0000000005.
[15] D. Gao, F. Scholten, B. Roldan Cuenya, Improved CO_2 electroreduction performance on plasma-activated Cu catalysts via electrolyte design: halide effect, ACS Catal. 7 (2017) 5112–5120, doi:10.1021/acscatal.7b01416.
[16] A. Tiwari, H.H. Heenen, A.S. Bjørnlund, T. Maagaard, E. Cho, I. Chorkendorff, H.H. Kristoffersen, K. Chan, S. Horch, Fingerprint voltammograms of copper single crystals under alkaline conditions: a fundamental mechanistic analysis, J. Phys. Chem. Lett. 11 (2020) 1450–1455, doi:10.1021/acs.jpclett.9b03728.
[17] Y. Huang, A.D. Handoko, P. Hirunsit, B.S. Yeo, Electrochemical reduction of CO_2 using copper single-crystal surfaces: effects of CO^* coverage on the selective formation of ethylene, ACS Catal. 7 (2017) 1749–1756, doi:10.1021/acscatal.6b03147.
[18] K.J.P. Schouten, E.P. Gallent, M.T.M. Koper, The electrochemical characterization of copper single-crystal electrodes in alkaline media, J. Electroanal. Chem. 699 (2013) 6–9, doi:10.1016/j.jelechem.2013.03.018.
[19] S. Grimme, J. Antony, S. Ehrlich, H. Krieg, A consistent and accurate ab initio parametrization of density functional dispersion correction (DFT-D) for the 94 elements H-Pu, J. Chem. Phys. 132 (2010) 154104, doi:10.1063/1.3382344.
[20] S. Grimme, S. Ehrlich, L. Goerigk, Effect of the damping function in dispersion corrected density functional theory, J. Comput. Chem. 32 (2011) 1456–1465, doi:10.1002/jcc.21759.
[21] J.P. Perdew, K. Burke, M. Ernzerhof, Generalized gradient approximation made simple, Phys. Rev. Lett. 77 (1996) 3865–3868, doi:10.1103/PhysRevLett.77.3865.
[22] G. Kresse, J. Furthmüller, Efficient iterative schemes for ab initio total-energy calculations using a plane-wave basis set, Phys. Rev. B 54 (1996) 11169–11186, doi:10.1103/PhysRevB.54.11169.
[23] J.H. Stenlid, M. Soldemo, A.J. Johansson, C. Leygraf, M. Göthelid, J. Weissenrieder, T. Brinck, Reactivity at the $Cu_2O(100)$:Cu–H_2O interface: a combined DFT and PES study, Phys. Chem. Chem. Phys. 18 (2016) 30570–30584, doi:10.1039/C6CP04410G.
[24] L. Bengtsson, Dipole correction for surface supercell calculations, Phys. Rev. B 59 (1999) 12301–12304, doi:10.1103/PhysRevB.59.12301.
[25] J.K. Nørskov, J. Rossmeisl, A. Logadottir, L. Lindqvist, J.R. Kitchin, T. Bligaard, H. Jónsson, Origin of the overpotential for oxygen reduction at a fuel-cell cathode, J. Phys. Chem. B 108 (2004) 17886–17892, doi:10.1021/jp047349j.

[26] S. Trasatti, The absolute electrode potential: an explanatory note (Recommendations 1986), Pure Appl. Chem. 58 (1986) 955–966, doi:10.1351/pac198658070955.
[27] J. Rossmeisl, K. Chan, R. Ahmed, V. Tripković, M.E. Björketun, pH in atomic scale simulations of electrochemical interfaces, Phys. Chem. Chem. Phys. 15 (2013) 10321–10325, doi:10.1039/C3CP51083B.
[28] M.W. Chase, C.A. Davies, J.R. Downey, D.J. Frurip, R.A. McDonald, A.N. Syverud, NIST-JANAF Thermochemical Tables, https://janaf.nist.gov/ (accessed March 2, 2019).
[29] P.E. Blöchl, Projector augmented-wave method, Phys. Rev. B 50 (1994) 17953–17979, doi:10.1103/PhysRevB.50.17953.
[30] G. Kresse, D. Joubert, From ultrasoft pseudopotentials to the projector augmented-wave method, Phys. Rev. B 59 (1999) 1758–1775, doi:10.1103/PhysRevB.59.1758.
[31] M. Methfessel, A.T. Paxton, High-precision sampling for Brillouin-zone integration in metals, Phys. Rev. B 40 (1989) 3616–3621, doi:10.1103/PhysRevB.40.3616.
[32] R.M. Arán-Ais, F. Scholten, S. Kunze, R. Rizo, B. Roldan Cuenya, The role of in situ generated morphological motifs and Cu(i) species in C_{2+} product selectivity during CO_2^- pulsed electroreduction, Nat. Energy 5 (2020) 317–325, doi:10.1038/s41560-020-0594-9.
[33] T. Schiros, S. Haq, H. Ogasawara, O. Takahashi, H. Öström, K. Andersson, L.G.M. Pettersson, A. Hodgson, A. Nilsson, Structure of water adsorbed on the open Cu(110) surface: H-up, H-down, or both? Chem. Phys. Lett. 429 (2006) 415–419, doi:10.1016/j.cplett.2006.08.048.
[34] K. Andersson, G. Ketteler, H. Bluhm, S. Yamamoto, H. Ogasawara, L.G.M. Pettersson, M. Salmeron, A. Nilsson, Bridging the pressure gap in water and hydroxyl chemistry on metal surfaces: the Cu(110) case, J. Phys. Chem. C 111 (2007) 14493–14499, doi:10.1021/jp073681u.
[35] N. Elgrishi, K.J. Rountree, B.D. McCarthy, E.S. Rountree, T.T. Eisenhart, J.L. Dempsey, A practical beginner's guide to cyclic voltammetry, J. Chem. Educ. 95 (2018) 197–206, doi:10.1021/acs.jchemed.7b00361.
[36] J. Smith, Z. Qin, F. King, L. Werme, D.W. Shoesmith, Sulfide film formation on copper under electrochemical and natural corrosion conditions, Corrosion 63 (2007) 135–144, doi:10.5006/1.3278338.
[37] N. Smart, B. Reddy, D. Nixon, A. Rance, A.J. Johansson, Miniature Canister (MiniCan) Corrosion Experiment Progress Report 5 for 2008–2013, Swedish Nuclear Fuel and Waste Management Co, 2014 P-14-19.
[38] F. King, M. Kolar, M. Vähänen, C. Lilja, Modelling long term corrosion behaviour of copper canisters in KBS-3 repository, Corros. Eng. Sci. Technol. 46 (2011) 217–222, doi:10.1179/18211Y.0000000004.
[39] J.M. Smith, J.C. Wren, M. Odziemkowski, D.W. Shoesmith, The electrochemical response of preoxidized copper in aqueous sulfide solutions, J. Electrochem. Soc. 154 (2007) C431–C438, doi:10.1149/1.2745647.
[40] I. Zaafarany, H. Boller, Corrosion of copper electrode in sodium sulfide solution, J. Saudi Chem. Soc. 14 (2010) 183–189, doi:10.1016/j.jscs.2010.02.019.
[41] C. Fiaud, M. Safavi, J. Vedel, Identification of the corrosion products formed on copper in sulfur containing environments, Mater. Corros. 35 (1984) 361–366, doi:10.1002/maco.19840350802.
[42] M. Guo, J. Chen, T. Martino, M. Biesinger, J.J. Noël, D.W. Shoesmith, The susceptibility of copper to pitting corrosion in borate-buffered aqueous solutions containing chloride and sulfide, J. Electrochem. Soc. 166 (2019) C550, doi:10.1149/2.0611915jes.
[43] F. King, C. Lilja, Localised corrosion of copper canisters, Corros. Eng. Sci. Technol. 49 (2014) 420–424.
[44] T. Martino, J. Chen, J.J. Noël, D.W. Shoesmith, The effect of anions on the anodic formation of copper sulphide films on copper, Electrochim. Acta (2019) 135319, doi:10.1016/j.electacta.2019.135319.
[45] T. Martino, R. Partovi-Nia, J. Chen, Z. Qin, D.W. Shoesmith, Mechanisms of film growth on copper in aqueous solutions containing sulphide and chloride under voltammetric conditions, Electrochim. Acta 127 (2014) 439–447, doi:10.1016/j.electacta.2014.02.050.
[46] J. Chen, Z. Qin, T. Martino, D.W. Shoesmith, Effect of chloride on Cu corrosion in anaerobic sulphide solutions, Corros. Eng. Sci. Technol. 52 (2017) 40–44, doi:10.1080/1478422X.2016.1271161.
[47] M. Pourbaix, Atlas of Electrochemical Equilibria in Aqueous Solutions, Pergamon Press, Oxford, 1966.
[48] F. King, D.S. Hall, P.G. Keech, Nature of the near-field environment in a deep geological repository and the implications for the corrosion behaviour of the container, Corros. Eng. Sci. Technol. 52 (2017) 25–30, doi:10.1080/1478422X.2017.1330736.
[49] F. King, C. Lilja, K. Pedersen, P. Pitkänen, M. Vähänen, An Update of the State-of-the-Art Report on the Corrosion of Copper Under Expected Conditions in a Deep Geologic Repository, Swedish Nuclear Fuel and Waste Management Co, 2010 TR-10-67.
[50] J.H. Stenlid, E. Campos dos Santos, A.J. Johansson, L.G.M. Pettersson, On the nature of the cathodic reaction during corrosion of copper in anoxic sulfide solutions, J. Electrochem. Soc. 166 (2019) C196–C208, doi:10.1149/2.0951906jes.
[51] C. Sena, J. Salas, D. Arcos, Aspects of Geochemical Evolution of the SKB Near Field in the Frame of SR-Site, Swedish Nuclear Fuel and Waste Management Co, 2010 TR-10-59.
[52] M. Laaksoharju, M. Gimeno, L. Auqué, J. Gómez, J. Smellie, E.-L. Tullborg, I. Gurban, Hydrogeochemical Evaluation of the Forsmark Site, Swedish Nuclear Fuel and Waste Management Co, 2004 Model Version 1.1, R-04-05.
[53] E. Protopopoff, P. Marcus, Potential–pH diagrams for sulfur and hydroxyl adsorbed on copper surfaces in water containing sulfides, sulfites or thiosulfates, Corros. Sci. 45 (2003) 1191–1201, doi:10.1016/S0010-938X(02)00210-X.
[54] M. Guo, J. Chen, T. Martino, C. Lilja, A.J. Johansson, M. Behazin, W.J. Binns, P.G. Keech, J.J. Noël, D.W. Shoemisth, The nature of the copper sulfide film grown on copper in aqueous sulfide and chloride solutions, Mater. Corros. (2020), doi:10.1002/maco.202011710.